Liang *et al. Microstructures* **2025**, *5*, 2025071
DOI: 10.20517/microstructures.2024.152

Microstructures

Research Article

Open Access

Nonvolatile multistate memories in $BiFeO_3$-based nanocomposites designed by phase-field simulations

Huan Liang[1,#], Yajing Liu[1,#], Yang Zhang[1], Dong Li[1], Sijia Song[1], Xinmiao Huang[1], Weiwei Li[1,2]

[1]College of Physics, MIIT Key Laboratory of Aerospace Information Materials and Physics, State Key Laboratory of Mechanics and Control for Aerospace Structures, Nanjing University of Aeronautics and Astronautics, Nanjing 211106, Jiangsu, China.
[2]College of Integrated Circuits, MIIT Key Laboratory of Aerospace Integrated Circuits and Microsystem, Nanjing University of Aeronautics and Astronautics, Nanjing 211106, Jiangsu, China.
[#]These authors contribute equally to this work.

Correspondence to: Dr. Yang Zhang, College of Physics, MIIT Key Laboratory of Aerospace Information Materials and Physics, State Key Laboratory of Mechanics and Control for Aerospace Structures, Nanjing University of Aeronautics and Astronautics, #29 Jiangjun Road, Jiangning District, Nanjing 211106, Jiangsu, China. E-mail: zhangyang919@nuaa.edu.cn; Prof. Weiwei Li, College of Physics, MIIT Key Laboratory of Aerospace Information Materials and Physics, State Key Laboratory of Mechanics and Control for Aerospace Structures, Nanjing University of Aeronautics and Astronautics, #29 Jiangjun Road, Jiangning District, Nanjing 211106, Jiangsu, China; College of Integrated Circuits, MIIT Key Laboratory of Aerospace Integrated Circuits and Microsystem, Nanjing University of Aeronautics and Astronautics, #29 Jiangjun Road, Jiangning District, Nanjing 211106, Jiangsu, China. E-mail: wl337@nuaa.edu.cn

How to cite this article: Liang, H.; Liu, Y.; Zhang, Y.; Li, D.; Song, S.; Huang, X.; Li, W. Nonvolatile multistate memories in $BiFeO_3$-based nanocomposites designed by phase-field simulations. *Microstructures* **2025**, *5*, 2025071. https://dx.doi.org/10.20517/microstructures.2024.152

Received: 9 Dec 2024 **First Decision:** 11 Mar 2025 **Revised:** 28 Mar 2025 **Accepted:** 8 Apr 2025 **Published:** 17 Jun 2025

Academic Editor: Zhanxi Fan **Copy Editor:** Shu-Yuan Duan **Production Editor:** Shu-Yuan Duan

Abstract

Realizing nonvolatile multiple polarization states in ferroelectric-based memories holds great promise for high-density data storage and advanced nanoelectronics. In this study, through phase-field simulations, we proposed a novel nonvolatile multistate memory design using $BiFeO_3$ (BFO)-dielectric nanocomposites to enhance storage density. By embedding BFO pillars within a dielectric matrix, we stabilized four distinct polarization states. The effects of pillar sizes and electric fields on the stability and switching behavior of these states were systematically investigated, showing that all four states can be effectively switched using either uniform electric fields or localized voltages via a piezoresponse force microscope tip. Simulations of a 4 × 4 memory cell array further highlighted the potential of this design, achieving a storage density far exceeding that of conventional ferroelectric random access memory devices. Our work shows the potential of ferroelectric-dielectric nanocomposites on high-density, rapidswitching nonvolatile memory technologies.

Keywords: Nonvolatile multistate memories, $BiFeO_3$, super-tetragonal phase, self-assembled nanocomposites, phase-field simulations

INTRODUCTION

Ferroelectric (FE) materials, characterized by their switchable spontaneous polarization, are widely used in information storage applications such as ferroelectric random access memory (FeRAM)[1,2]. Compared to other nonvolatile memory technologies, FE-based devices offer several advantages, including fast read/write operations, low power consumption, and exceptional durability[3,4]. However, traditional FeRAM technology is constrained by limited data storage capacity, hindering their further integration in advanced computing systems[5]. To address this challenge, one promising strategy involves increasing the number of saturated polarization states within a single unit, thereby enabling multiple memory states per cell beyond the conventional binary states of “0” and “1”[6]. This strategy not only enhances storage density but also holds promise for neuromorphic computing applications in today’s era of big data and artificial intelligence[4,7].

Considering various domains in FE materials, one approach to achieving multiple polarization states is to control the stepwise domain switching pathways under external electric fields[8-12]. For example, intermediate polarization values have been achieved by modulating up/down polarization ratios in $PbZr_{1-x}Ti_xO_3$ (PZT) thin film[9]. Similarly, multiple thermodynamically stable twinning structures can form in (111)-oriented PZT films during the ferroelastic switching process[11]. While these methods can produce abundant states under varying electric fields, precise control over these polarization values remains challenging. Another approach focuses on creating regions with distinct polarization behaviors under electric fields by modifying material composition, introducing defects, or adjusting external conditions[13-15]. For instance, $Pb_{1-x}Sr_xTiO_3$ exhibits varying coercive fields based on strontium contents; hence, a bilayer with different compositions results in an in-plane (IP) four-state switching accompanied by interlayer coupling[14]. However, this approach may compromise long-term device reliability due to the potential degradation of interfacial couplings. The third approach leverages inherent multiple polarization states within single FE materials[16,17]. Research on (110)-oriented $BiFeO_3$ (BFO) films has demonstrated a three-state switching[16]. While this method promises improved stability and scalability, such a system remains limited for practical computational usage due to its incompatibility with the binary architecture.

In fact, many FE materials exhibit multiple symmetrical phases, such as PZT near its morphotropic phase boundary (MPB)[18,19]. Nevertheless, stabilizing individual phases via electric fields is challenging, and the work to utilize inherent multiple phases for multistate memory applications remains largely unexplored.

BFO, a multiferroic material displaying both ferroelectricity and antiferromagnetism at room temperature[20,21], is a prominent candidate for next-generation nanoelectronics. Its notable properties, such as large remnant polarization and strong coupling between ferroic orders, make it an ideal platform for exploring multistate memory applications[22]. In addition to a rhombohedral (R) phase, BFO also exhibits a super-tetragonal (T^S) phase characterized by a large polarization value and a high c/a ratio[23]. Figure 1A illustrates the free energy landscape of BFO. The color on the spherical surface indicates the minimal energy density along the corresponding directional angle. As shown in the left panel of Figure 1A, under stress-free conditions, both R and T^S phases are present. However, the T^S phase exhibits significantly higher energy than that of the R phase, rendering the T^S phase unstable and prone to transitioning to the R phase. It should also be noted that the T^S phase does not possess tetragonal symmetry but rather monoclinic

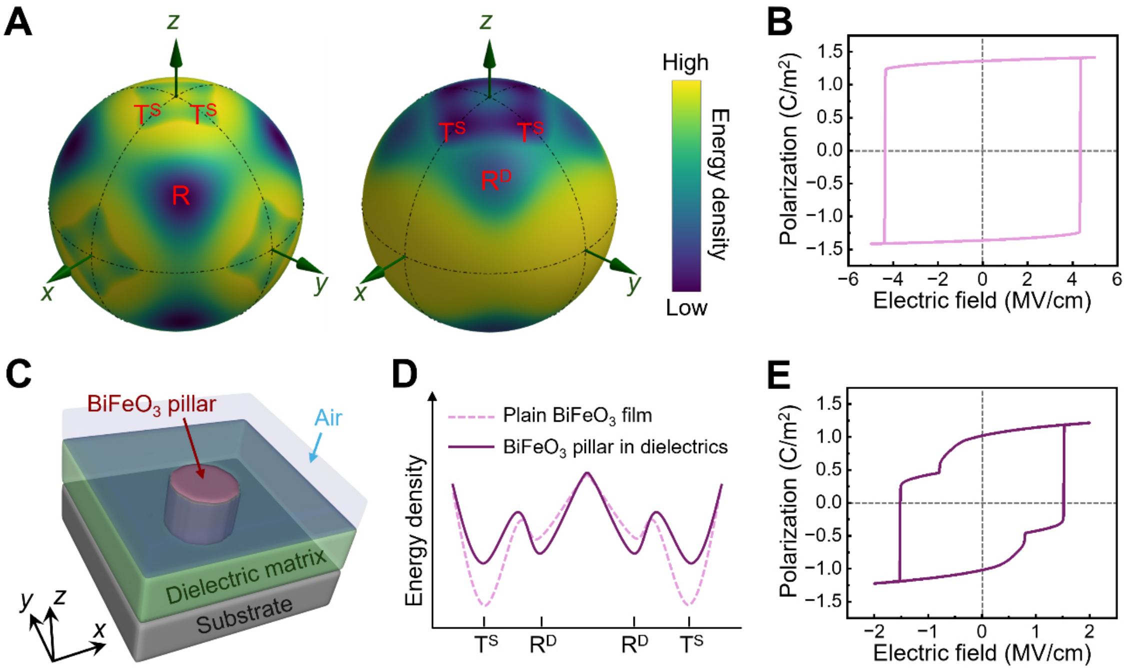

Figure 1. Design of multistate BFO nanocomposites. (A) Polar plots of free energies for BFO under stress-free conditions (left) and under an IP compressive strain of -1.3% combined with an OOP tensile stress of 9.12 GPa (right). The right panel is similar to the case of a high in-plane compressive strain of -4%, demonstrating comparable stabilization of the super-tetragonal phase; (C) Schematic of the proposed nanocomposite structure consisting of a substrate layer, a film layer of a BFO pillar surrounded by a dielectric matrix, and an air layer; (D) Designed energy density profiles of a plain BFO film and a BFO pillar embedded in a dielectric matrix; (E) Electric hysteresis loop of the designed BFO nanocomposite film. BFO: $BiFeO_3$; IP: in-plane; OOP: out-of-plane.

symmetry[24,25], while its out-of-plane (OOP) polarization is substantially larger (~ 1.4 C/m^2) compared to the R phase (~ 0.6 C/m^2)[25]. When subjected to large IP compressive strain and/or OOP tensile stress, the T^S phase becomes energetically favorable, whereas the R phase is constrained to the distorted rhombohedral (R^D) phase and becomes metastable. The right panel of Figure 1A shows the case under IP compressive strain of -1.3% and OOP tensile stress of 9.12 GPa (equals to a tensile mismatch of 4%), and it is similar to the one under IP strain of -4%. In this scenario, strain-induced phase separation allows the coexistence of both R^D and T^S phases[23,26,27], presenting an opportunity to stabilize four distinct polarization states.

Despite its potential, plain BFO films under large IP compressive strain cannot maintain a single R phase due to intrinsic constraints. Figure 1B presents the polarization-electric field (*P-E*) hysteresis loop of plain BFO films subjected to an IP strain of -4%. The resulting square-shaped loop highlights the inability to stabilize the R phase under these conditions, which impedes the direct utilization of high-strained BFO films for achieving multiple polarization states.

In recent years, self-assembled ferroelectric/dielectric nanocomposites have attracted considerable attention for their potential in advanced nanotechnologies[28]. These nanocomposites provide enhanced control over the functions of FE phases, offering a versatile platform for the design of multistate memory systems[29]. Specifically, vertically aligned nanocomposites have demonstrated notable improvements in the ferroelectric, piezoelectric, and dielectric properties of functional materials[30,31], while also enhancing overall stability. These characteristics make them promising candidates for stabilizing both the R^D and T^S phases in BFO films, thereby enabling the realization of multistate memory devices.

In this study, we propose a novel structure in which a BFO circular pillar is embedded within a dielectric matrix [Figure 1C]. The tensile stress arising from the larger lattice constants of the matrix promotes the stabilization of the T^S phase[31]. In addition, careful interface engineering may lead to similar energy minima for both R^D and T^S phases [Figure 1D], facilitating the stabilization of each single phase. Using phase-field simulations, we successfully stabilize four distinct states in this configuration [Figure 1E], thereby demonstrating its potential for high-density memory applications.

METHODS

In this study, we employed a phase-field model to explore the polarization dynamics and multistate design of BFO/dielectric nanocomposites. The polarization vector P_i (i = 1, 2, 3) was chosen as the order parameter. The total free energy can be written as[32]:

$$F = \int_V \left(f_{\text{Land}} + f_{\text{grad}} + f_{\text{elas}} + f_{\text{elec}} \right) \mathrm{d}V \tag{1}$$

where f_{Land}, f_{grad}, f_{elas}, and f_{elec} represent the volume densities of Landau free energy, gradient energy, elastic energy, and electrostatic energy, respectively.

The Landau free energy density is extended to eighth order to describe both the R and T^S phases:

$$\begin{aligned} f_{\text{Land}} = {} & \alpha_1 \left(P_1^2 + P_2^2 + P_3^2 \right) + \alpha_{11} \left(P_1^4 + P_2^4 + P_3^4 \right) + \alpha_{12} \left(P_1^2 P_2^2 + P_2^2 P_3^2 + P_3^2 P_1^2 \right) \\ & + \alpha_{111} \left(P_1^6 + P_2^6 + P_3^6 \right) + \alpha_{112} \left[P_1^4 \left(P_2^2 + P_3^2 \right) + P_2^4 \left(P_3^2 + P_1^2 \right) + P_3^4 \left(P_1^2 + P_2^2 \right) \right] \\ & + \alpha_{123} P_1^2 P_2^2 P_3^2 + \alpha_{1111} \left(P_1^8 + P_2^8 + P_3^8 \right) \\ & + \alpha_{1112} \left[P_1^6 \left(P_2^2 + P_3^2 \right) + P_2^6 \left(P_3^2 + P_1^2 \right) + P_3^6 \left(P_1^2 + P_2^2 \right) \right] \\ & + \alpha_{1122} \left(P_1^4 P_2^4 + P_2^4 P_3^4 + P_3^4 P_1^4 \right) + \alpha_{1123} \left(P_1^4 P_2^2 P_3^2 + P_1^2 P_2^4 P_3^2 + P_1^2 P_2^2 P_3^4 \right) \end{aligned} \tag{2}$$

where α_1, α_{11}, α_{12}, α_{111}, α_{112}, α_{123}, α_{1111}, α_{1112}, α_{1122}, and α_{1123} are the Landau polynomial coefficients.

The gradient energy density, arising from the discontinuity of order parameters and accounting for the contribution of interfaces, is given by:

$$\begin{aligned} f_{\text{grad}} = {} & \frac{1}{2} G_{11} \left(P_{1,1}^2 + P_{2,2}^2 + P_{3,3}^2 \right) + G_{12} \left(P_{1,1} P_{2,2} + P_{2,2} P_{3,3} + P_{3,3} P_{1,1} \right) \\ & + \frac{1}{2} G_{44} \left[\left(P_{1,2} + P_{2,1} \right)^2 + \left(P_{2,3} + P_{3,2} \right)^2 + \left(P_{3,1} + P_{1,3} \right)^2 \right] \\ & + \frac{1}{2} G'_{44} \left[\left(P_{1,2} - P_{2,1} \right)^2 + \left(P_{2,3} - P_{3,2} \right)^2 + \left(P_{3,1} - P_{1,3} \right)^2 \right] \end{aligned} \tag{3}$$

where G_{11}, G_{12}, G_{44}, and G_{44} are the gradient energy density coefficients, and $P_{i,j}$ denotes $\partial P_i / \partial x_j$ with x_j as the spatial coordinate.

The elastic energy density, describing the interactions between strain and stress, is expressed as:

$$f_{\text{elas}} = \frac{1}{2} c_{ijkl} \left(\varepsilon_{ij} - \varepsilon_{ij}^0 \right) \left(\varepsilon_{kl} - \varepsilon_{kl}^0 \right) \tag{4}$$

where c_{ijkl} is the elastic stiffness tensor, ε_{ij} is the total strain, and $\varepsilon^0_{ij} = Q_{ijkl}P_kP_l$ is the eigenstrain with Q_{ijkl} as the electrostrictive coefficients. The Einstein notation is used.

The electrostatic energy density is:

$$f_{\text{elec}} = -E_iP_i - \frac{1}{2}\varepsilon_0\kappa_{\text{b}}E_iE_i \tag{5}$$

where $E_i = - \partial\varphi / \partial x_i$ is the electric field with φ as the electrostatic potential, ε_0 is the permittivity of vacuum, and κ_{b} is the background relative permittivity of materials.

The time evolution of the order parameters is governed by the time-dependent Ginzburg-Landau (TDGL) equations:

$$\frac{\partial P_i}{\partial t} = -L_P\frac{\delta F}{\delta P} \tag{6}$$

where L_P is the kinetic coefficient. The TDGL equations are solved using the semi-implicit Fourier spectral method[33]. For each step, the elastic and electric driving forces are determined by solving the mechanical equilibrium equations $\sigma_{ij,j} = 0$ and the electrostatic equilibrium equation $D_{i,i} = 0$, where $\sigma_{ij} = c_{ijkl}(\varepsilon_{ij} - \varepsilon^0_{ij})$ is the local stress and $D_i = \varepsilon_0\kappa_{\text{b}}E_i + P_i$ is the electric displacement. The superposition method is employed to solve film boundary conditions[34,35].

The mechanical boundary conditions are mixed, i.e., $\varepsilon_{11} = \varepsilon_{22} = \varepsilon_s$, $\varepsilon_{12} = \varepsilon_{21} = 0$, and $\sigma_{33} = \sigma_{13} = \sigma_{31} = \sigma_{23} = \sigma_{32} = 0$, where ε_s is the IP strain imposed by substrate[34]. The electric boundary conditions are closed-circuit[36]. The potential of the bottom film-substate interface is set to zero. Under a uniform electric field, the potential on the top surface is also uniform. If applying a piezoresponse force microscopy (PFM) tip, the surface potential distribution follows a two-dimensional Lorentz-like function[37,38]:

$$\varphi_{\text{top}}(x_1, x_2) = \varphi_0\left[\frac{\gamma^2}{\left(x_1 - x_1^0\right)^2 + \left(x_2 - x_2^0\right)^2 + \gamma^2}\right] \tag{7}$$

where φ_0 is the applied potential, i.e., the maximal potential, γ is the length of half-maximum potential, and (x_1^0, x_2^0) is the tip location.

In our simulations, we assumed that the substrate material is $SrTiO_3$ (STO) and the surrounding dielectric material is MgO. Based on the lattice constants of these materials (BFO: 3.96 Å, STO: 3.91 Å, and MgO: 4.21 Å) and setting BFO as the reference, the IP strain is -1.3%, and the mismatch strain of MgO is 4% (lower than the theoretical 6.3% based on lattice constants) to account for dislocation-induced strain relaxation at BFO-MgO interfaces[39]. For BFO, according to previous literature[27], $\alpha_1 = 4.184 \times 10^5 \times (T - 1123.5)$ $\text{C}^{-2}\text{m}^2\text{N}$ with $T = 298$ (in Kelvin) as the ambient temperature, $\alpha_{11} = 2.127 \times 10^9$ $\text{C}^{-4}\text{m}^6\text{N}$, $\alpha_{12} = -2.049 \times 10^9$ $\text{C}^{-4}\text{m}^6\text{N}$, $\alpha_{111} = -1.76 \times 10^9$ $\text{C}^{-6}\text{m}^{10}\text{N}$, $\alpha_{112} = 8.298 \times 10^8$ $\text{C}^{-6}\text{m}^{10}\text{N}$, $\alpha_{123} = 3.358 \times 10^9$ $\text{C}^{-6}\text{m}^{10}\text{N}$, $\alpha_{1111} = 3.92 \times 10^8$ $\text{C}^{-8}\text{m}^{14}\text{N}$, $\alpha_{1112} = 4.400 \times 10^7$ $\text{C}^{-8}\text{m}^{14}\text{N}$, $\alpha_{1122} = -3.8 \times 10^8$ $\text{C}^{-8}\text{m}^{14}\text{N}$, $\alpha_{1123} = 8 \times 10^8$ $\text{C}^{-8}\text{m}^{14}\text{N}$, $c_{11} = 228$ GPa, $c_{12} = 128$ GPa, $c_{44} = 65$ GPa, and $\kappa_{\text{b}} = 40$. For MgO, $_1 = 5.0 \times 10^9$ $\text{C}^2\text{m}^2\text{N}$, $\alpha_{11} = \alpha_{12} = \alpha_{111} = \alpha_{112} = \alpha_{123} = \alpha_{1111} = \alpha_{1112} = \alpha_{1122} = \alpha_{1123} = 0$, $c_{11} = 293$ GPa, $c_{12} = 92$ GPa, $c_{44} = 155$ GPa, and $\kappa_{\text{b}} = 10$. For STO, $c_{11} = 228$ GPa, $c_{12} = 128$ GPa, and $c_{44} = 65$ GPa. Voigt notation is used. Additionally, $Q_{11} = 0.071$ C^{-2}m^4, $Q_{12} = -0.030$ C^{-2}m^4, $Q_{44} = -0.295$ C^{-2}m^4, $G_{11} = 1.2G_{110}$, $G_{12} = 0$, and $G_{44} = G'_{44} = 0.6G_{110}$, where $G_{110} = 3.45410^{-10}$ $\text{C}^{-2}\text{m}^4\text{N}$. The spectral iterative perturbation method is used[40]. For a PFM tip, the location (x_1^0, x_2^0) is at the center of the BFO pillar, and $\gamma = 3.0$ nm.

The size of one unit case is $64\Delta x \times 64\Delta x \times 40\Delta x$ with $\Delta x = 0.4$ nm, including 15 layers for the substrate and 15 layers for the BFO-MgO film, as illustrated in Figure 1C. The size of the 4 × 4 cell array is $200\Delta x \times 200\Delta x \times 40\Delta x$, as shown below.

RESULTS AND DISCUSSION

Stability of four states

Using the phase-field model, we first examined the stability of the four potential polarization states by varying the diameter of the BFO pillars. Figure 2A shows the *P-E* loops for BFO-MgO systems with different BFO pillar diameters (*d*) under an electric field of 2 MV/cm. For larger pillar diameters (*d* = 12 nm), the results resemble those of plain BFO films [Figure 1B], albeit with a significant reduction in the coercive field due to the influence of the dielectric interfaces.

In plain strained BFO films, the T^S phase typically exhibits much lower elastic energy compared to the R^D phase, despite having higher Landau free energy. However, in BFO-MgO nanocomposites, the low permittivity of surrounding dielectrics leads to reduced polarization even under high fields. This causes substantial gradient and depolarization interactions in the vicinity of the BFO/MgO interfaces. To minimize these energies, the BFO dipoles near interfaces tend to decrease their magnitudes and align parallel to the interfaces. Similar behaviors have been observed in $PbTiO_3/SrTiO_3$ superlattices near FE/dielectric interface[41]. As a result, the T^S phases with large polarization are less favored near the interfaces, thereby lowering the energy barrier between up and down polarizations of the T^S phases. Conversely, the R^D phases, which exhibit relatively smaller polarization, are more stable near the interfaces. Therefore, at *d* = 12 nm, intermediate R^D phases appear during the polarization switching, although this effect is subtle.

As the pillar diameter decreases, the surface-to-volume ratio increases, enhancing the stability of the R^D phase. When the diameter was reduced to 8 nm, both the R^D and T^S phases were found to be stable. At even smaller diameters, the T^S phase becomes metastable; it appears only when an electric field is applied. For pillar diameters smaller than 4 nm, the T^S phase could no longer be stabilized under the applied electric field.

Figure 2B illustrates the four distinct polarization states at *d* = 8 nm, with these states being referred to as +H, +L, -H, and -L for simplicity. They correspond to the T^S phase (+H and -H) and the R^D phase (+L and -L). By extracting two specific points from the *P-E* loop at *d* = 8 nm (indicated by purple triangles) and allowing the system to relax after removing the external electric field, we confirmed the stability of both phases over time [Figure 2C]. From an energy perspective, the total energy density of the two phases is comparable, consistent with our designed energy landscape shown in Figure 1D.

Further analysis revealed that the diameter of the BFO pillars significantly influences phase stability. For *d* = 6 nm, the T^S phase under zero electric field is unstable due to large gradient and Landau energy contributions [Figure 2D, left panel]. In contrast, for *d* = 12 nm, the initial R^D phase quickly transitions to the T^S phase due to the dominance of elastic energy [Figure 2D, right panel]. These findings emphasize the critical role of BFO/MgO interfaces, governed by pillar size, in balancing the free energy contributions and stabilizing desired phases. For subsequent investigations, we selected *d* = 8 nm as the optimal pillar diameter.

Switching dynamics among four states

Having confirmed the stability of the four polarization states, we next examined the switching dynamics among these states under pulsed electric fields. Here, we use $+E^H$, $+E^L$, $-E^L$, and $-E^H$ to represent the fields of

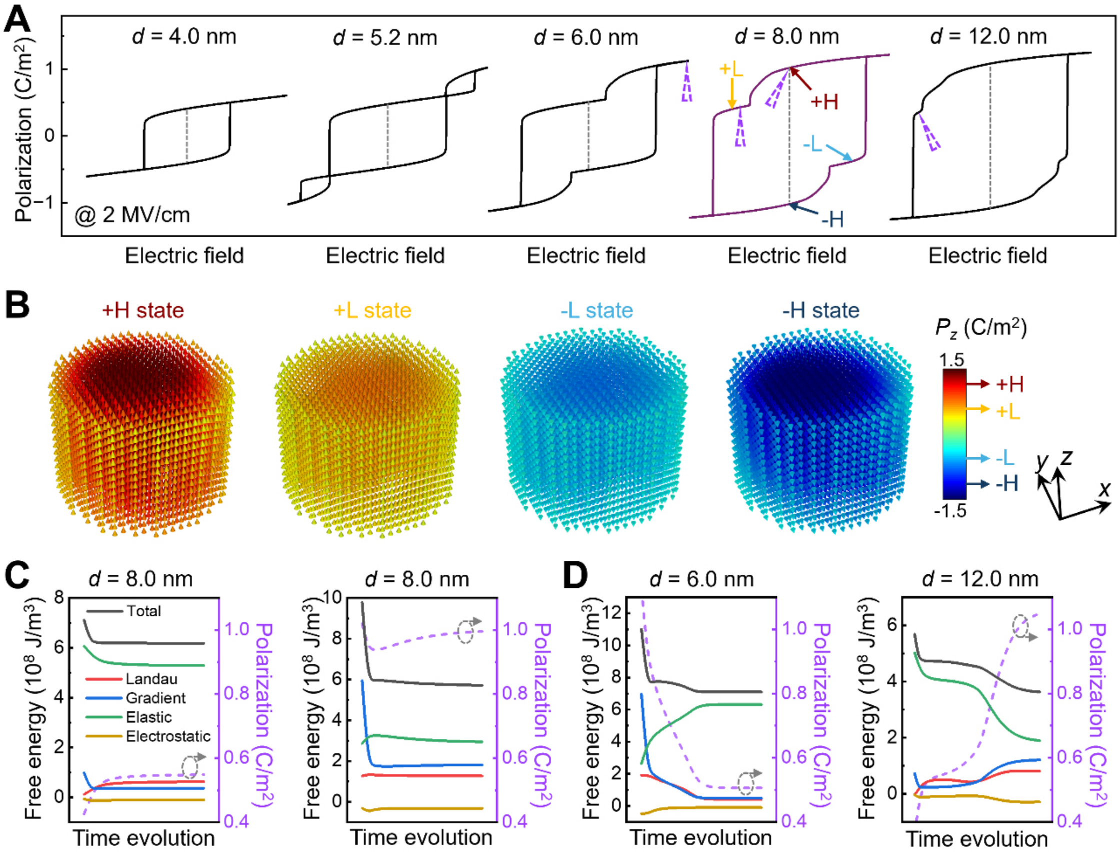

Figure 2. Influence of pillar size on phase stability. (A) Electric hysteresis loops of BFO pillar films at 2 MV/cm for various pillar diameters *d*; (B) Three-dimensional polarization vectors corresponding to four stable states for *d* = 8 nm. The vector colors represent the magnitude of out-of-plane polarization P_z; (C and D) Free energy densities and polarization evolution for *d* = 8 nm; (C) and for *d* = 6 nm and 12 nm (D) from specific states in the hysteresis loops indicated by purple triangles in (A) under zero electric field. BFO: BiFeO$_3$ OOP: out-of-plane.

+1.8, +1, -1, and -1.8 MV/cm, respectively. Figure 3A shows the polarization evolution as a function of the pulsed electric field, indicating that all four states can be easily switched and stabilized by applying external electric fields of diferent directions and magnitudes. Figure 3B summarizes all the possible switching routes between every two states.

To assess the potential for localized control, we also conducted simulations using a PFM tip. We found that applying voltages of ± 1.2V and ± 0.6V corresponded to the electric fields of $\mp E^{H}$ and $\mp E^{L}$, respectively. These results validate the feasibility of precise and flexible control over the polarization states.

For practical implementation, we propose two approaches to achieve transitions from any starting state to all four states, as shown in Figure 3C. For the first approach, an external $+E^{H}$ field is applied to initialize the system in the +H state. The -H and +L states can then be obtained by applying the $-E^{H}$ and $-E^{L}$ fields, respectively. To reach the -L state, an additional $+E^{L}$ field is applied to the -H state. The second approach involves applying $+E^{H}$ and $-E^{H}$ fields to establish the +H and -H states, respectively. The +L and -L states can then be achieved by applying the $-E^{L}$ and $+E^{L}$ fields, respectively.

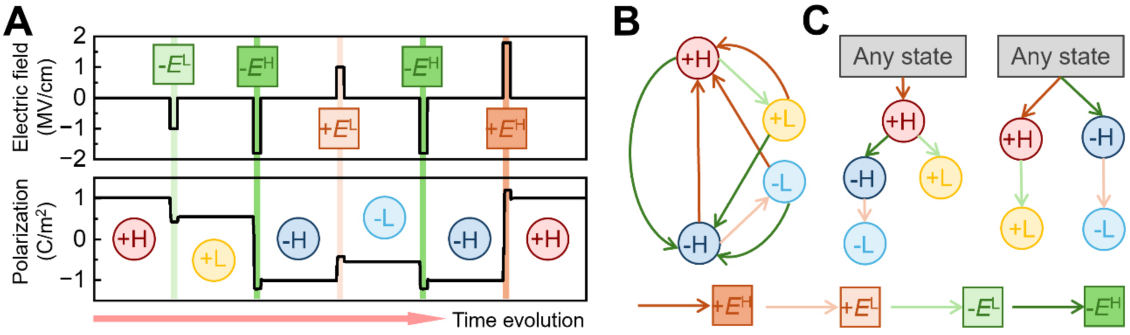

Figure 3. Switching dynamics between multiple states. (A) Polarization evolution as a function of external pulsed electric field; (B) Schematical illustration of all possible switching routes between the four stable states controlled by electric fields; (C) Two proposed approaches to obtaining all states from any initial state.

To quantify the energy barrier between states, we then analyzed the switching fields and found that E^L ranges from 0.7 to 1.4 MV/cm, while E^H should be at least 1.5 MV/cm. Considering the polarization values of H and L states(~ 1.0 and 0.5 C/m^2), the energy density barrier between two adjacent high/low states (e.g., +H to +L) is estimated as $P \cdot E^L \approx 3.5 \times 10^7$ J/m^3, while transitions between opposite states (e.g., +H to -H) require $P \cdot E^H \approx 3.0 \times 10^8$ J/m^3. Assuming a cell volume of ~ 300 nm^3 (IP diameter d = 8 nm and film thickness h = 6 nm), the estimated switching energy per operation is ~ 10^{-5} to 10^{-4} pJ, suggesting ultralow power consumption compared to conventional FeRAM. This is primarily due to the nanoscale size of memory cells, though practical implementations would require further integration with transistor-based architecture.

A demonstration of cell array

To demonstrate the potential for high-density data storage, we also simulated a 4 × 4 memory cell array using the proposed multistate memory design. The layout of the proposed array is shown in Figure 4A. Each cell has a diameter of 8 nm, with a spacing of 12 nm between adjacent cells, sufficiently avoiding the interactions between neighboring cells. To switch a specific cell, a PFM tip is applied at the center of the targeted cell with an appropriate voltage.

By encoding the four polarization states as binary bits (“00”, “01”, “10”, and “11” correspond to +H, +L, -L, and -H states, respectively), the storage density is effectively doubled. This allows for more data to be stored within the same physical area [Figure 4B]. For example, knowing that storing one ASCII character requires 8 bits, four ASCII characters can be stored in 16 cells with the proposed design, instead of 32 cells by traditional designs.

Figure 4C shows the successful switching process of individual cells in the 4 × 4 array to store desired information in Figure 4B. We first applied a uniform +E^H field, initializing all cells in the “00” states. Individual cells are then switched to the desired states sequentially using the PFM tip, following a switching process of zero, one, or two steps, as outlined in the left panel of Figure 3C. For example, the first binary-bit cell was applied by a voltage of 0.6 V, switching to the “01” state. The second cell was already in the desired “00” state and did not require additional manipulation. The third cell underwent a sequential voltage application of 1.2 V, followed by -0.6 V, ultimately reaching the “11” state. After a series of steps, the designed information configuration was successfully achieved. This array configuration (pillar diameter d = 8 nm and center-to-center distance of adjacent pillar is 20 nm) results in each cell occupying 400 nm^2. With 2-bit/cell encoding, the theoretical storage density is 2 bit / 400 nm^2 = 500 Gbit/cm^2. This value remarkably surpasses the storage capacity of traditional FeRAM devices, though practical limitations such as read/write

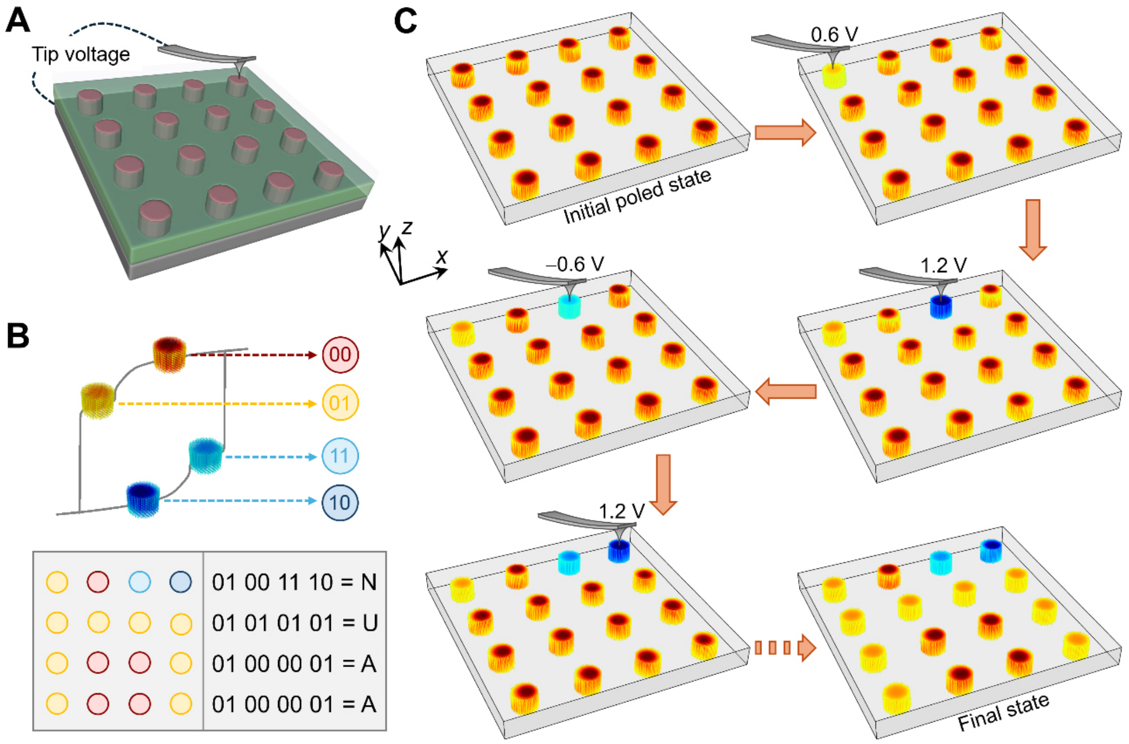

Figure 4. Demonstration of data writing in a 4 × 4 cell array. (A) Simulated structure of a 4 × 4 cell array, each cell 20 nm × 20 nm with BFO pillar diameter of 8 nm. The switching process is performed using a PFM tip; (B) Design of data storage, where each 8-bit ASCII character is stored by four cells; (C) Phase-field simulation of the data writing process in (B), beginning from an initial poled state with all cells in the "00" state, and then writing each cell sequentially by one or two steps. BFO: $BiFeO_3$; PFM: piezoresponse force microscopy.

circuitry and thermal stability may reduce the achievable densities.

CONCLUSIONS

In conclusion, we have proposed an innovative design for nonvolatile multistate memories based on BFO-dielectric nanocomposites. Using phase-field simulations, we successfully demonstrated the stabilization and switching of four distinct polarization states. By carefully optimizing the size of the BFO pillars, both the R^D and T^S phases could be stabilized through the subtle balance of free energies, especially the gradient and elastic energy terms. These polarization states can be effectively switched by applying external electric fields or localized voltages via a PFM tip. Low energy consumption and large polarization contrast ensure low-cost and reliable read/write operations. Additionally, our simulation of a 4 × 4 memory cell array illustrates the potential for high-density data storage, offering substantial advantages over traditional FeRAM devices. However, interfacial fatigue during cycling, multistep write operations, and the trade-off between applied voltage and leakage in nanocomposite films remain critical challenges, requiring materials engineering and interfacial optimization. This work not only provides a novel approach for boosting the capacity of FE-based memory devices but also opens up new possibilities for designing next-generation electronic nanotechnologies. Future research could extend this approach to other materials, such as other perovskite ferroelectrics like $PbTiO_3$(exhibiting T^S phases under strain), solid solutions like PZT near MPBs (enabling rhombohedral and tetragonal phase coexistence), and van der Waals materials like $CuInP_2S_6$ (with quadruple-well polarization potentials[15,42,43]), to further optimize data capabilities and switching flexibility.

DECLARATIONS

Acknowledgement

The authors acknowledge Beijng PARATERA Tech CO.,Ltd. for providing HPC resources that have contributed to the researh results reported within this paper (https://www.paratera.com/).

Authors' contributions

Design: Zhang, Y.; Li, W.
Simulation: Liang, H.; Liu, Y.; Zhang, Y.
Data analysis: Liang, H.; Li, D.; Song, S.; Huang, X.
Manuscript writing: Liang, H.; Liu, Y.; Zhang, Y.
Manuscript revision and supervision: Li, W.
All authors have read and agreed to the published version of the manuscript.

Availability of data and materials

The data that support the findings of this study are available from the corresponding authors upon reasonable request.

Financial support and sponsorship

This work was supported by the National Natural Science Foundation of China (Grant Nos. 92477107, 52302184, and 52102177). Y.Z. is also grateful for funding support from the State Key Laboratory of New Ceramic and Fine Processing Tsinghua University (Grant No. KF202308). Weiwei Li is also grateful for funding support from the National Natural Science Foundation of Jiangsu Province (Grant No. BK20210313), the Fundamental Research Funds for the Central Universities (Grant Nos. NS2023057 and NI2023001), the Research Fund of State Key Laboratory of Mechanics and Control for Aerospace Structures (Nanjing University of Aeronautics and Astronautics) (Grant No. MCAS-I-0424G02), funding for Stable Support for Basic Research Projects of National Defense Characteristics (Grant No. ILF240031A24), Top-notch Academic Programs Project of Jiangsu Higher Education Institutions (TAPP), and the Jiangsu Specially-Appointed Professor Program.

Conflicts of interest

All authors declared that there are no conflicts of interest.

Ethical approval and consent to participate

Not applicable.

Consent for publication

Not applicable.

Copyright

REFERENCES

1. Auciello, O.; Scott, J. F.; Ramesh, R. The physics of ferroelectric memories. *Phys. Today.* **1998**, *51*, 22-7. DOI
2. Setter, N.; Damjanovic, D.; Eng, L.; et al. Ferroelectric thin films: review of materials, properties, and applications. *J. Appl. Phys.* **2006**, *100*, 051606. DOI
3. Arimoto, Y.; Ishiwara, H. Current status of ferroelectric random-access memory. *MRS. Bull.* **2004**, *29*, 823-8. DOI
4. Sebastian, A.; Le, G. M.; Khaddam-Aljameh, R.; Eleftheriou, E. Memory devices and applications for in-memory computing. *Nat. Nanotechnol.* **2020**, *15*, 529-44. DOI
5. Kent, A. D.; Worledge, D. C. A new spin on magnetic memories. *Nat. Nanotechnol.* **2015**, *10*, 187-91. DOI PubMed
6. Cao, Q.; Lü, W.; Wang, X. R.; et al. Nonvolatile multistates memories for high-density data storage. *ACS. Appl. Mater. Interfaces.*

2020, *12*, 42449-71. DOI

7. Wu, S.; Zhang, X.; Cao, R.; et al. Multi-state nonvolatile capacitances in HfO_2-based ferroelectric capacitor for neuromorphic computing. *Appl. Phys. Lett.* **2024**, *124*, 102902. DOI
8. Lee, D.; Jeon, B. C.; Baek, S. H.; et al. Active control of ferroelectric switching using defect-dipole engineering. *Adv. Mater.* **2012**, *24*, 6490-5. DOI
9. Lee, D.; Yang, S. M.; Kim, T. H.; et al. Multilevel data storage memory using deterministic polarization control. *Adv. Mater.* **2012**, *24*, 402-6. DOI
10. Vasudevan, R. K.; Matsumoto, Y.; Cheng, X.; et al. Deterministic arbitrary switching of polarization in a ferroelectric thin film. *Nat. Commun.* **2014**, *5*, 4971. DOI
11. Xu, R.; Liu, S.; Saremi, S.; et al. Kinetic control of tunable multi-state switching in ferroelectric thin films. *Nat. Commun.* **2019**, *10*, 1282. DOI PubMed PMC
12. Wang, G.; Hu, T.; Zhu, W.; et al. Multiple local symmetries result in a common average polar axis in high-strain $BiFeO_3$-based ceramics. *Phys. Rev. Lett.* **2023**, *130*, 076801. DOI
13. Saremi, S.; Xu, R.; Allen, F. I.; et al. Local control of defects and switching properties in ferroelectric thin films. *Phys. Rev. Mater.* **2018**, 2. DOI
14. Kavle, P.; Ross, A. M.; Zorn, J. A.; et al. Exchange-interaction-like behavior in ferroelectric bilayers. *Adv. Mater.* **2023**, *35*, e2301934. DOI
15. Li, T.; Wu, Y.; Yu, G.; et al. Realization of sextuple polarization states and interstate switching in antiferroelectric $CuInP_2S_6$. *Nat. Commun.* **2024**, *15*, 2653. DOI PubMed PMC
16. Lee, J. H.; Chu, K.; Kim, K.; Seidel, J.; Yang, C. Out-of-plane three-stable-state ferroelectric switching: finding the missing middle states. *Phys. Rev. B.* **2016**, 93. DOI
17. Liu, L.; Cai, Y.; Chen, X.; Liu, Z.; Yuan, G.; Wang, Y. Flexible multi-state nonvolatile antiferroelectric memory. *J. Am. Ceram. Soc.* **2022**, *105*, 6232-40. DOI
18. Noheda, B.; Cox, D. E.; Shirane, G.; Gonzalo, J. A.; Cross, L. E.; Park, S. A monoclinic ferroelectric phase in the $Pb(Zr_{1-x}Ti_x)O_3$ solid solution. *Appl. Phys. Lett.* **1999**, *74*, 2059-61. DOI
19. Noheda, B.; Cox, D. E.; Shirane, G.; Guo, R.; Jones, B.; Cross, L. E. Stability of the monoclinic phase in the ferroelectric perovskite $PbZr_{1-x}Ti_xO_3$. *Phys. Rev. B.* **2000**, 63. DOI
20. Wang, J.; Neaton, J. B.; Zheng, H.; et al. Epitaxial $BiFeO_3$ multiferroic thin film heterostructures. *Science* **2003**, *299*, 1719-22. DOI
21. Eerenstein, W.; Mathur, N. D.; Scott, J. F. Multiferroic and magnetoelectric materials. *Nature* **2006**, *442*, 759-65. DOI PubMed
22. Catalan, G.; Scott, J. F. Physics and applications of bismuth ferrite. *Adv. Mater.* **2009**, *21*, 2463-85. DOI
23. Zeches, R. J.; Rossell, M. D.; Zhang, J. X.; et al. A strain-driven morphotropic phase boundary in $BiFeO_3$. *Science* **2009**, *326*, 977-80. DOI
24. Christen, H. M.; Nam, J. H.; Kim, H. S.; Hatt, A. J.; Spaldin, N. A. Stress-induced R-M_A-M_C-T symmetry changes in $BiFeO_3$ films. *Phys. Rev. B.* **2011**, 83. DOI
25. Rossell, M. D.; Erni, R.; Prange, M. P.; et al. Atomic structure of highly strained $BiFeO_3$ thin films. *Phys. Rev. Lett.* **2012**, *108*, 047601. DOI
26. You, L.; Chen, Z.; Zou, X.; et al. Characterization and manipulation of mixed phase nanodomains in highly strained $BiFeO_3$ thin films. *ACS. Nano.* **2012**, *6*, 5388-94. DOI
27. Xue, F.; Li, Y.; Gu, Y.; Zhang, J.; Chen, L. Strain phase separation: formation of ferroelastic domain structures. *Phys. Rev. B.* **2016**, 94. DOI
28. Macmanus-driscoll, J. L. Self-assembled heteroepitaxial oxide nanocomposite thin film structures: designing interface-induced functionality in electronic materials. *Adv. Funct. Mater.* **2010**, *20*, 2035-45. DOI
29. Zhao, R.; Yang, C.; Wang, H.; et al. Emergent multiferroism with magnetodielectric coupling in $EuTiO_3$ created by a negative pressure control of strong spin-phonon coupling. *Nat. Commun.* **2022**, *13*, 2364. DOI PubMed PMC
30. MacManus-Driscoll, J. L.; Wu, R.; Li, W. Interface-related phenomena in epitaxial complex oxide ferroics across different thin film platforms: opportunities and challenges. *Mater. Horiz.* **2023**, *10*, 1060-86. DOI PubMed PMC
31. Zhang, L.; Chen, J.; Fan, L.; et al. Giant polarization in super-tetragonal thin films through interphase strain. *Science* **2018**, *361*, 494-7. DOI
32. Chen, L. Phase-field models for microstructure evolution. *Annu. Rev. Mater. Res.* **2002**, *32*, 113-40. DOI
33. Chen, L.; Shen, J. Applications of semi-implicit Fourier-spectral method to phase field equations. *Comput. Phys. Commun.* **1998**, *108*, 147-58. DOI
34. Li, Y.; Hu, S.; Liu, Z.; Chen, L. Effect of substrate constraint on the stability and evolution of ferroelectric domain structures in thin films. *Acta. Materialia.* **2002**, *50*, 395-411. DOI
35. Li, Y. L.; Chen, L. Q.; Asayama, G.; Schlom, D. G.; Zurbuchen, M. A.; Streiffer, S. K. Ferroelectric domain structures in $SrBi_2Nb_2O_9$ epitaxial thin films: electron microscopy and phase-field simulations. *J. Appl. Phys.* **2004**, *95*, 6332-40. DOI
36. Li, Y. L.; Hu, S. Y.; Liu, Z. K.; Chen, L. Q. Effect of electrical boundary conditions on ferroelectric domain structures in thin films. *Appl. Phys. Lett.* **2002**, *81*, 427-9. DOI
37. Choudhury, S.; Zhang, J. X.; Li, Y. L.; Chen, L. Q.; Jia, Q. X.; Kalinin, S. V. Effect of ferroelastic twin walls on local polarization switching: Phase-field modeling. *Appl. Phys. Lett.* **2008**, *93*, 162901. DOI

38. Gao, P.; Britson, J.; Nelson, C. T.; et al. Ferroelastic domain switching dynamics under electrical and mechanical excitations. *Nat. Commun.* **2014**, *5*, 3801. DOI
39. Chen, A.; Hu, J. M.; Lu, P.; et al. Role of scaffold network in controlling strain and functionalities of nanocomposite films. *Sci. Adv.* **2016**, *2*, e1600245. DOI PubMed PMC
40. Wang, J.; Ma, X.; Li, Q.; Britson, J.; Chen, L. Phase transitions and domain structures of ferroelectric nanoparticles: Phase field model incorporating strong elastic and dielectric inhomogeneity. *Acta. Materialia.* **2013**, *61*, 7591-603. DOI
41. Yadav, A. K.; Nelson, C. T.; Hsu, S. L.; et al. Observation of polar vortices in oxide superlattices. *Nature* **2016**, *530*, 198-201. DOI
42. Zhou, S.; You, L.; Zhou, H.; Pu, Y.; Gui, Z.; Wang, J. Van der Waals layered ferroelectric CuInP2S6: Physical properties and device applications. *Front. Phys.* **2021**, *16*, 986. DOI
43. Meng, P.; Wu, Y.; Bian, R.; et al. Sliding induced multiple polarization states in two-dimensional ferroelectrics. *Nat. Commun.* **2022**, *13*, 7696. DOI PubMed PMC